PERGAMON

International Journal of Heat and Mass Transfer 45 (2002) 3331–3347

International Journal of HEAT and MASS TRANSFER

www.elsevier.com/locate/ijhmt

# Effect of surface radiation on conjugate mixed convection in a vertical channel with a discrete heat source in each wall

C. Gururaja Rao [1], C. Balaji, S.P. Venkateshan *

*Heat Transfer and Thermal Power Laboratory, Department of Mechanical Engineering, Indian Institute of Technology, Chennai 600 036, India*

Received 15 June 2001; received in revised form 21 January 2002

**Abstract**

The results of a numerical analysis of the problem of two-dimensional, steady, incompressible, conjugate, laminar, mixed convection with surface radiation in a vertical parallel-plate channel, provided with a flush-mounted, heat generating, discrete heat source in each wall, are presented here. Air, a radiatively non-participating medium, is used as the cooling agent. A computer code based on the finite volume method is written exclusively for solving the above problem. The effect of surface emissivity, aspect ratio, discrete heat source position and modified Richardson number on the fluid flow and heat transfer characteristics is explored. Useful correlations are evolved for the maximum temperature of the left and the right channel walls, the mean friction coefficient and the forced convection component of the mean friction coefficient. 

## 1. Introduction

A vertical parallel-plate channel is a commonly encountered configuration in applications like the cooling of electronic equipment, transformers, transistors and main frame computers. The nature of heat dissipation from the channel walls mainly varies with the packaging constraints and the operation modes of the specific device or system. Though the use of a symmetric or asymmetric isothermal or isoflux wall boundary condition may provide an acceptable accuracy in the first-cut evaluation of the thermal performance in a majority of applications, a more realistic analysis would involve the presence of heat generating discrete heat sources in the channel walls. This results in multi-mode heat transfer, with conduction along the walls, convection (free and forced) and surface radiation from the surfaces of the walls, in all those cases, which make use of air (or any other transparent gas) as the cooling medium.

Ever since Elenbaas [1] came out with his benchmark paper, presenting the experimental results of free convection in a parallel-isothermal plate channel using air as the cooling medium, several analytical, numerical and experimental analyses involving the geometry of a vertical channel have been reported in the literature. Some examples include Tao [2], Bar-Cohen and Rohsenow [3] and Barletta [4]. Most of the above mentioned studies have considered the analysis of mixed convection alone. However, in practice, in a majority of situations there is interaction between different modes of heat transfer. This makes it mandatory to solve a coupled heat transfer problem. Literature provides quite a few studies pertaining to multi-mode heat transfer in several geometries, with Dehghan and Behnia [5] and Gururaja Rao et al. [6] being some of the examples. However, for the geometry of a vertical channel, analyses concerning multi-mode heat transfer are very scarce. First among the examples for the above include Anand et al. [7], who studied, numerically, the effect of wall conduction on free convection between asymmetrically heated vertical plates, for the case of uniform wall temperatures. Kim et al. [8] numerically solved the same problem for the case of uniform wall heat flux. Kim et al. [9] also made a numerical analysis of laminar free convection in

* Corresponding author.
*E-mail address:* spv35@hotmail.com (S.P. Venkateshan).
[1] Department of Mechanical Engineering, Regional Engineering College, Warangal 506 004 (AP), India.

0017-9310/02/$ - see front matter 
PII: S0017-9310(02)00061-3

**Nomenclature**

$A, A_{g_1}, A_{g_2}$ aspect ratio and two other geometric ratios, $(L/S), (S/t)$ and $(S/L_h)$, respectively

$A_1, A_2$ non-dimensional positions of the left and the right wall discrete heat sources, $(L_1/S)$ and $(L_2/S)$, respectively

$\overline{C}_f$ mean friction coefficient based on both the channel walls, $\overline{C}_f$ (Left) + $\overline{C}_f$ (Right)

$\overline{C}_f$ (Left) left wall mean friction coefficient, $(1/A)(2/Re_S)\int_0^A (\partial U/\partial Y)_{Y=0}\,dX$

$\overline{C}_f$ (Right) right wall mean friction coefficient, $(1/A)(2/Re_S)\int_0^A (\partial U/\partial Y)_{Y=1}\,dX$

$F_{ij}$ view factor from the $i$th element to the $j$th element of an enclosure

$g$ acceleration due to gravity, 9.81 m/s$^2$

$Gr_S^*$ modified Grashof number based on $S$, $g\beta\Delta T_{ref}S^3/\nu^2$

$H$ height of the computational domain, m

$J$ radiosity, W/m$^2$

$J'$ dimensionless radiosity, $J/\sigma T_\infty^4$

$k$ thermal conductivity, W/m K

$L, t, S$ height, thickness and spacing of the walls of the channel, respectively, m

$L_h$ height of each of the discrete heat sources, m

$L_1, L_2$ positions of the left and the right wall discrete heat sources, respectively, m

$M, N, N_1$ number of grid points in $Y$ and $X$ directions and along the channel, respectively

$n$ total number of elements along the enclosure used in radiation analysis

$N_{RF}$ radiation-flow interaction parameter, $\sigma T_\infty^4/((k_f/S)\Delta T_{ref})$

$P$ pressure at any location in the computational domain, Pa

$Pe_S$ Peclet number based on $S$, $u_\infty S/\alpha$

$q_{R,i}$ radiation heat flux from any element (for $\varepsilon_i \neq 1$) $(\varepsilon_i/1-\varepsilon_i)(\sigma T_i^4 - J_i)$, W/m$^2$

$q_V$ volumetric heat generation rate in each discrete heat source, W/m$^3$

$Q_C$ net convection heat transfer rate in the channel, $Q_C$ (Left) + $Q_C$ (Right), W/m

$Q_C$ (Left) left wall convection heat transfer rate, $-k_f\Delta T_{ref}\int_0^A (\partial\theta/\partial Y)_{Y=0}\,dX$, W/m

$Q_C$ (Right) right wall convection heat transfer rate, $-k_f\Delta T_{ref}\int_0^A (\partial\theta/\partial Y)_{Y=1}\,dX$, W/m

$Q_R$ net radiation heat transfer rate in the channel, $Q_R$ (Left) + $Q_R$ (Right), W/m

$Q_R$ (Left/Right) radiation heat transfer rate from the left or the right wall, $S\int_0^A q_{R,i}\,dX$, W/m

$Q$ total heat transfer rate in the channel, $(Q_C + Q_R)$, W/m

$Re_S$ Reynolds number based on $S$, $u_\infty S/\nu$

$Ri_S^*$ modified Richardson number based on $S$, $(Gr_S^*/Re_S^2)$ or $g\beta\Delta T_{ref}S/u_\infty^2$

$T$ temperature at any location in the computational domain, K

$T_\infty, u_\infty$ fluid temperature and velocity at the channel entrance, K and m/s, respectively

$u$ vertical velocity, m/s

$U$ non-dimensional vertical velocity, $u/u_\infty$ or $\partial\psi/\partial Y$

$v$ horizontal or cross velocity, m/s

$V$ non-dimensional horizontal or cross velocity, $v/u_\infty$ or $-\partial\psi/\partial X$

$x, y$ vertical and horizontal distances, respectively, m

$X, Y$ non-dimensional vertical and horizontal distances, $x/S, y/S$, respectively

*Greek symbols*

$\alpha$ thermal diffusivity of air, m$^2$/s

$\beta$ isobaric cubic expansivity of air, $-(1/\rho)(\partial\rho/\partial T)_P$ $(K^{-1})$

$\delta$ convergence criterion, in percentage, $|(\zeta_{new}-\zeta_{old})/\zeta_{new}| \times 100\%$

$\Delta T_{ref}$ modified reference temperature difference, $(q_V L_h t/k_s)$, K

$\Delta x$ height of the wall element chosen for energy balance, m

$\Delta X$ non-dimensional height of the wall element chosen for energy balance, $\Delta x/S$

$\varepsilon$ surface emissivity of any wall of the channel or any element of an enclosure

$\gamma$ non-dimensional thermal conductivity parameter, $k_f S/k_s t$

$\nu$ kinematic viscosity of air, m$^2$/s

$\omega'$ vorticity, s$^{-1}$

$\omega$ non-dimensional vorticity, $\omega' S/u_\infty$

$\rho$ density of the fluid, kg/m$^3$

$\sigma$ Stefan-Boltzmann constant, $5.6697 \times 10^{-8}$ W/ m$^2$ K$^4$

$\psi'$ stream function, m$^2$/s

$\psi$ non-dimensional stream function, $\psi'/u_\infty S$

$\theta$ non-dimensional temperature, $(T - T_\infty)/\Delta T_{ref}$

$\theta_{av}$ non-dimensional average left or right wall temperature, $(1/A)\int_0^A \theta_W\,dX$

$\zeta$ any dependent variable ($\psi, \omega$ or $\theta$), over which convergence is being tested for

*Subscripts*

| | |
|---|---|
| f, s | fluid (air) and solid (material of the channel wall), respectively |
| *i*, *j* | any two arbitrary elements of an enclosure used in radiation analysis |
| L, R | left and right walls of the channel, respectively |
| new, old | values of any variable from the current and previous iterations, respectively |
| W, max, av | local, maximum and average values of the wall temperature, respectively |

channels formed between series of vertical parallel plates with embedded line heat sources. Watson et al. [10] performed a numerical study of laminar mixed convection between a series of vertically aligned parallel plates with planar heat sources.

A careful review of literature reveals that enough attention has not been given to the interaction of surface radiation with mixed (combined free and forced) convection in a channel. Also no study has considered the analysis of conjugate mixed convection with surface radiation in a vertical channel provided with heat generating discrete heat sources in both the walls. Hence a numerical study of conjugate mixed convection with surface radiation in a vertical channel, provided with a flush-mounted heat generating discrete heat source in each wall, with air as the cooling medium, is made in this paper.

### 1.1. Mathematical formulation

The governing equations for two-dimensional, steady, incompressible, laminar, mixed convection in a vertical parallel-plate channel, for a constant property fluid with the Boussinesq approximation assumed to be valid, are available in a number of references, e.g., [11]. The schematic of the problem geometry, along with the system of coordinates, consisting of a vertical parallel-plate channel of height $L$ and width (or wall spacing) $S$, with each wall of thickness $t$, is shown in Fig. 1. The thermal conductivity and the surface emissivity of the two walls are the same and are equal to $k_s$ and $\varepsilon$, respectively. There are two flush-mounted discrete heat sources, one in each wall. The two heat sources are of equal height $L_h$ and they provide a symmetric and uniform volumetric heat generation at the rate of $q_V$. The left wall and the right wall heat source positions are $L_1$ and $L_2$, respectively, and $L_1$ need not be equal to $L_2$. Further, the heat sources may be located anywhere along the top, bottom and the left surfaces of the left wall and the top, bottom and the right surfaces of the right wall are adiabatic. The fluid enters from the bottom of the channel with a uniform velocity $u_\infty$ and a uniform temperature $T_\infty$. The governing equations are simplified, by converting them into the vorticity–stream function ($\omega$–$\psi$) form, and are later normalized. A modified reference temperature difference needs to be introduced for multimode problems like these. In this study $\Delta T_{ref} = q_V L_h t/k_s$. Temperature is non-dimensionalized as $\theta = (T - T_\infty)/\Delta T_{ref}$. The governing equations, in their final non-dimensional form, are:

Vorticity transport equation:

$$U\frac{\partial\omega}{\partial X} + V\frac{\partial\omega}{\partial Y} = -Ri_S^*\frac{\partial\theta}{\partial Y} + \frac{1}{Re_S}\left[\frac{\partial^2\omega}{\partial X^2} + \frac{\partial^2\omega}{\partial Y^2}\right]. \quad (1)$$

Stream function equation:

$$\frac{\partial^2\psi}{\partial X^2} + \frac{\partial^2\psi}{\partial Y^2} = -\omega. \quad (2)$$

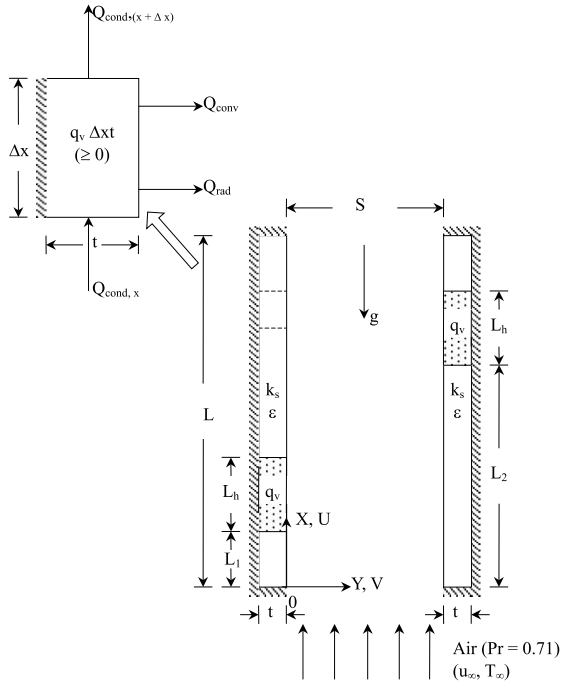


Fig. 1. Schematic of the problem geometry [inset showing an enlarged left wall element used for making the energy balance].

Energy equation:

$$U\frac{\partial\theta}{\partial X}+V\frac{\partial\theta}{\partial Y}=\frac{1}{Pe_S}\left[\frac{\partial^2\theta}{\partial X^2}+\frac{\partial^2\theta}{\partial Y^2}\right]. \tag{3}$$

The modified Richardson number ($Ri_S^*$) in Eq. (1) is based on the reference temperature difference given earlier.

### 1.2. Surface radiation calculations

The enclosure analysis, with radiosity-irradiation formulation for the evaluation of the radiosities of all the wall elements, is used for making surface radiation calculations. The general radiosity equation for the $i$th element of an enclosure may be written as:

$$J_i=\varepsilon_i\sigma T_i^4+(1-\varepsilon_i)\sum_{j=1}^{n}F_{ij}J_j \quad \text{for } [1\leqslant i\leqslant n]. \tag{4}$$

Here, $F_{ij}$ is the view factor from the $i$th element to the $j$th element of the enclosure, while n is the total number of elements along the enclosure. View factors are evaluated using Hottel's crossed string method [14].

### 1.3. Computational domain and boundary conditions

The computational domain in the present study is extended beyond the channel exit by a height equal to that of the channel ($L$), based on a study that will be presented later. The width of the computational domain is equal to the channel spacing $S=(L/A)$, where $A$ is the aspect ratio. At the bottom of the computational domain, since the velocity and the temperature of the fluid entering the channel are uniform and equal to $u_\infty$ and $T_\infty$, respectively, the appropriate boundary conditions are $(\partial\psi/\partial Y)=1$, $\omega=0$ and $\theta=0$. Along the left wall of the channel, the stream function ($\psi$) is constant and taken to be zero. For calculating the vorticity ($\omega$), the wall-vorticity equation, $\omega=-(\partial^2\psi/\partial Y^2)$, is used. Due to heat generation in the discrete heat source, which is accompanied by internal conduction and convection (free and forced) and radiation at the surface, the temperature $\theta$ varies along the left wall, and this is obtained as a part of the solution to the present problem. Along the extended left boundary, owing to symmetry, $V=0$, which means that $(\partial\psi/\partial X)=0$, implying $\psi$ is a constant. Since $\psi=0$ along the left wall, the same condition is continued along the extended left boundary also. The vorticity $\omega$ is 0 here. As there is no heat transfer across the extended left boundary, $(\partial\theta/\partial Y)=0$. Across the top of the computational domain, the fully-developed condition, $(\partial\psi/\partial X)=0$, is used for $\psi$, which seems justified on account of extension of the computational domain by a length equal to the channel height. For similar reasons, irrotationality condition is imposed here, resulting in $\omega=0$. When the vertical velocity $U$ is positive, the fully-developed condition, $(\partial\theta/\partial X)=0$, is used for $\theta$, and when $U$ is negative, implying an inward flow, $\theta=0$ is used, since the incoming fluid is considered to be at $T_\infty$. On the right wall, $\psi$, which would again be a constant, is taken equal to 1. For calculating $\omega$, the same wall-vorticity equation as used for the left wall, viz., $\omega=-(\partial^2\psi/\partial Y^2)$, is used. The temperature $\theta$ along the right wall, like that along the left wall, would come out as a part of the solution. The boundary conditions for the extended right boundary, based on similar arguments are $\psi=1,\omega=0$ and $(\partial\theta/\partial Y)=0$.

### 1.4. Temperature boundary condition along the left and right channel walls

The equation for temperature distribution along each of the two channel walls is derived based on an energy balance, and the inset to Fig. 1 shows an enlarged left wall element, chosen for this purpose, along with the various energy interactions that are involved. An energy balance on a left wall element on that portion of the wall that contains the heat source, results in

$$Q_{\text{cond},x}+q_V\Delta xt=Q_{\text{cond},(x+\Delta x)}+Q_{\text{conv}}+Q_{\text{rad}}. \tag{5}$$

The above equation, after the substitution of all the relevant expressions, simplification and non-dimensionalization, leads to the equation for temperature variation along that portion of the left wall, which possesses the discrete heat source (excluding the bottom and top ends), as

$$\frac{\partial^2\theta}{\partial X^2}+\gamma\left(\frac{\partial\theta}{\partial Y}\right)_{Y=0}+A_{g_1}A_{g_2}-\left(\frac{\varepsilon}{1-\varepsilon}\right)\gamma N_{\text{RF}}\times\left[\left(\frac{T}{T_\infty}\right)^4-J'\right]=0. \tag{6}$$

For the remainder of the left wall (which does not contain the discrete heat source), the third term in Eq. (6) is equal to zero.

Similarly for the right wall we have

$$\frac{\partial^2\theta}{\partial X^2}-\gamma\left(\frac{\partial\theta}{\partial Y}\right)_{Y=1}+A_{g_1}A_{g_2}-\left(\frac{\varepsilon}{1-\varepsilon}\right)\gamma N_{\text{RF}}\times\left[\left(\frac{T}{T_\infty}\right)^4-J'\right]=0. \tag{7}$$

Again, for the remaining portion of the right wall not possessing the heat source, the third term in Eq. (7) vanishes. Eqs. (6) and (7) get modified appropriately for the bottom and top adiabatic ends of the left and right

walls of the channel, depending on whether or not each of these ends form a part of the discrete heat source.

## 2. Method of solution

The governing equations (1)–(3) are converted into finite difference equations, using a finite-volume based finite difference method due to Gosman et al. [12]. The advection terms present in Eqs. (1) and (3) are handled using a second upwind scheme, the details of which are available in Roache [13]. The resulting algebraic equations are subsequently solved using the Gauss-Seidel iterative procedure. Under relaxation, with a relaxation parameter of 0.5, is used on vorticity and stream function, while full relaxation (relaxation parameter = 1.0) is used on temperature. A convergence criterion $\delta$ of 0.01% has been employed for vorticity, stream function and temperature.

Since the temperature varies along the length of the two walls of the channel, it is essential to discretize the computational domain such that the wall temperature distribution is properly simulated. It has to be ensured that there are always a certain minimum number of closely spaced grids near the entrance of the channel, from where the flow begins, and also adjacent to the walls of the channel, where the velocity and temperature gradients are steep. There should be a minimum number of finer grids along each of the two discrete heat sources since maximum variation of temperature occurs only here. It is required to have closer grids just before and immediately after each of the two discrete heat sources so as to avoid sudden changes in velocity and temperature gradients. In view of these prerequisites, a cosine function is chosen for generating the grids in the $Y$- direction. In the $X$-direction, along the wall of the channel, cosine grids are used from the entry of the channel to the beginning of the heat source, while semi-cosine grids are used along the heat sources. For the case, where the two heat sources are at different heights from the channel entry, cosine grids are used in between the two heat sources. Beyond the second one of the two heat sources, up to the channel exit, the same semi-cosine function as has been used along the second heat source is continued. In the extended region, uniform grids are used in the $X$-direction, while there is no change of grid pattern in the $Y$-direction. Thus, a special hybrid grid system, encompassing all the above features, has been designed. Fig. 2 shows the grid pattern used for the case, where the left wall heat source starts at the entry and the right wall heat source ends on the exit of the channel, along with all the boundary conditions used in the study.

The same non-uniform grid system, as used for convection calculations, is employed for the evaluation of the view factors and radiosities needed in calculating

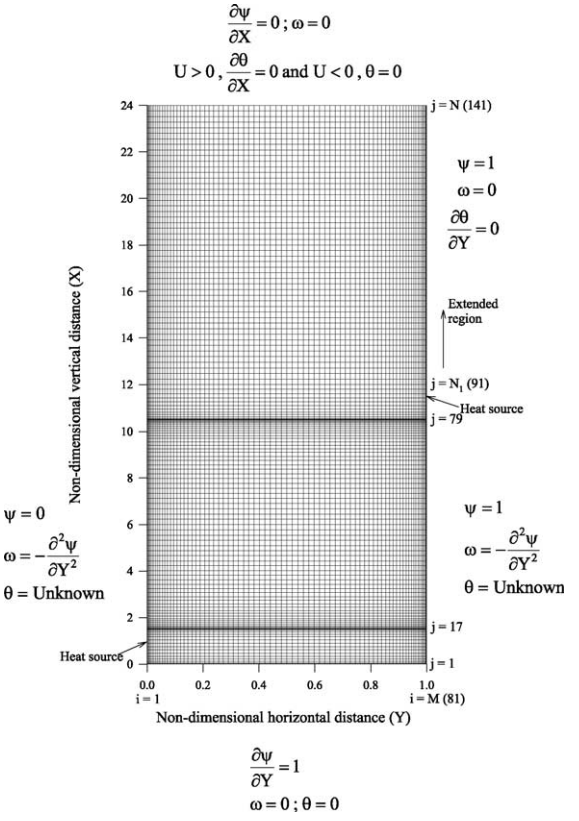


Fig. 2. A typical grid pattern used for the case where the left wall heat source is at the entry and the right wall heat source is at the exit of the channel along with the boundary conditions [$A = 12$, $L_1 = 0, L_2 = 7L/8$ and Grid size = $81 \times 141$].

the net radiation heat transfer and the wall temperatures, so as to ensure grid compatibility. All the open boundaries of the computational domain are assumed to be black and at a uniform temperature $T_\infty$, which is equal to the entry temperature of the fluid. The radiosities ($J$) of all the elements along the enclosure are obtained by solving, simultaneously, the radiosity equations, written for each of these elements as in Eq. (4).

The local velocities and temperatures in the entire computational domain (including the local left and right wall temperatures) are obtained as a part of the solution. The non-dimensional maximum temperature ($\theta_{\max}$) along each channel wall is determined from the local values of non-dimensional temperature along the appropriate walls. The non-dimensional average temperature ($\theta_{\text{av}}$) of each wall, the mean friction coefficient ($\overline{C}_{\text{f}}$) based on both the walls and the net rates of convection and radiation heat transfer are calculated using the expressions given in the nomenclature. Three-point formulae, using a second degree Lagrangian polynomial, are used for evaluating all the derivatives present in the boundary conditions and also the derivatives that are

Table 1
Range of parameters

| Parameter | Units |
|---|---|
| $4 \leqslant A \leqslant 20$ | – |
| $0 \leqslant A_1, A_2 \leqslant 17.5$ | – |
| $10^5 \leqslant q_V \leqslant 10^6$ | W/m$^3$ |
| $0.25 \leqslant k_s \leqslant 1$ | W/m K |
| $0.23 \leqslant \gamma \leqslant 4.6$ | – |
| $0.05 \leqslant N_{RF} \leqslant 10.25$ | – |
| $0.05 \leqslant \varepsilon_L, \varepsilon_R \leqslant 0.85$ | – |
| $15 \leqslant Re_S \leqslant 27500$ | – |
| $0.1 \leqslant Ri_S^* \leqslant 25$ | – |

Air ($Pr = 0.71$), $T_\infty = 25$ °C, $L = 233.4$ mm, $t = 1.5$ mm and $L_h = 29.2$ mm.

needed in the rest of the calculations. The integrations needed in all the calculations are performed using an extended Simpson's 1/3 rule for non-uniform step sizes.

All the calculations in the present analysis are done for air ($Pr = 0.71$), assuming it to be a radiatively transparent, Boussinesq fluid. The range of parameters used in the present work is listed in Table 1. The height of the channel ($L$) is taken to be 233.4 mm, which is the typical height of a PCB (printed circuit board), used in electronic applications. The wall thickness ($t$) is taken to be 1.5 mm, while the height ($L_h$) of each discrete heat source is taken to be equal to $L/8$ (29.175 mm). The channel spacing $S$ depends on the aspect ratio $A$, the range ($4 \leqslant A \leqslant 20$) for which was decided based on some of the experimental studies reported on electronic equipment cooling, reported in Peterson and Ortega [15]. The range ($0.05 \leqslant \varepsilon \leqslant 0.85$) is chosen for the surface emissivity of each wall, keeping in mind two typical surfaces (polished aluminum, with $\varepsilon = 0.05$, and black paint, with $\varepsilon = 0.85$) used in practice. The range for wall thermal conductivity ($k_s$) is taken to be ($0.25 \leqslant k_s \leqslant 1$) because PCBs are typically made of materials with a thermal conductivity of the order of unity (e.g., Mylar coated epoxy glass, with $k_s = 0.25$ W/m K). The range ($0.1 \leqslant Ri_S^* \leqslant 25$) is chosen appropriate for $Ri_S^*$ from the point of view of the maximum wall temperature, which is found to go beyond 120 °C for $Ri_S^*$ greater than 25 (asymptotic free convection limit), while it goes below 30 °C for $Ri_S^*$ less than 0.1 (asymptotic forced convection limit). Keeping in mind that, in most of the applications, the maximum wall temperature ranges between 30 and 120 °C, the above range for $Ri_S^*$ seems to be quite appropriate.

## 3. Results and discussion

### 3.1. Grid independence test

The effect of grid size ($M \times N$) on the present problem is studied by considering a typical case with $A = 12, A_1 = A_2 = 5.25$ (heat sources at the respective wall centers), $k_s = 0.25$ W/m K, $q_V = 10^6$ W/m$^3$, $\varepsilon = 0.45$, $Ri_S^* = 1, Re_S = 1070$ and $Gr_S^* = 1.15 \times 10^6$. The results are summarized in Table 2. The grid independence is tested in two stages: (1) $M$ is fixed and $N$ is varied and (2) $N$ is fixed and $M$ is varied. It is to be noted that, since, in the present example, the left and the right wall heat sources are at the same position in their respective walls, the non-dimensional maximum temperature ($\theta_{max}$) would be the same for both the walls. The results of the first stage (with $M$ fixed) indicate that the difference in $\theta_{max}$ between the grid sizes $81 \times 141$ and $81 \times 161$ is 0.0004%, while the difference in $\overline{C}_f$ between the same two grid sizes is 0.006%. The results of the second stage (with $N$ fixed) reveal that the difference in $\theta_{max}$ between the grid sizes $81 \times 141$ and $101 \times 141$ is 0.01%, while for $\overline{C}_f$, the difference is 0.76%. In view of the above, $M$ and $N$ have been fixed as 81 and 141, respectively. In the above study, the number of grids along the channel is taken to be 90 (i.e., $N_1 = 91$). This, in fact, is based on another study for the same example as above, and the results are provided in Table 3. It can be seen that the difference in $\theta_{max}$ between $N_1 = 71$ and 91 is 0.04%, while that between $N_1 = 91$ and 111 is 0.02%. With regard to $\overline{C}_f$, the difference between $N_1 = 71$ and 91 is 0.52% and that between $N_1 = 91$ and 111 is 0.35%. Thus, $N_1$ (the number of nodes along the channel) is fixed as 91. Hence, all the subsequent calculations in the present study are per-

Table 2
Grid independence test – to fix $M$ and $N$

| Stage | Grid size ($M \times N$) | $\theta_{max}$ (Left/Right) | Percentage change (abs.) | $\overline{C}_f$ | Percentage change (abs.) |
|---|---|---|---|---|---|
| (1) $M = 81$, $N$ varied | 81×121 | 0.248148 | – | 0.048141 | – |
| | 81×141 | 0.248142 | 0.002 | 0.048136 | 0.01 |
| | 81×161 | 0.248141 | 0.0004 | 0.048133 | 0.006 |
| (2) $N = 141$, $M$ varied | 61×141 | 0.249330 | – | 0.049329 | – |
| | 81×141 | 0.248142 | 0.48 | 0.048136 | 2.41 |
| | 101×141 | 0.248175 | 0.01 | 0.047768 | 0.76 |

$A = 12, A_1 = A_2 = 5.25$ (heat sources at wall centers), $q_V = 10^6$ W/m$^3$, $\varepsilon = 0.45, k_s = 0.25$ W/m K, $k_f = 0.0291$ W/m K, $Ri_S^* = 1, Re_S = 1070, Gr_S^* = 1.15 \times 10^6$ ($N_1 = 91$).

Table 3
Grid independence test – to fix $N_1$

| $N_1$ | $\theta_{max}$ (Left/Right) | Percentage change (abs.) | $\overline{C}_f$ | Percentage change (abs.) |
|---|---|---|---|---|
| 71 | 0.248036 | – | 0.048392 | – |
| 91 | 0.248142 | 0.04 | 0.048136 | 0.52 |
| 111 | 0.248098 | 0.02 | 0.048305 | 0.35 |

$A = 12, A_1 = A_2 = 5.25$ (heat sources at wall centers), $q_V = 10^6$ W/m$^3$, $\varepsilon = 0.45, k_s = 0.25$ W/m K, $k_f = 0.0291$ W/m K, $Ri_S^* = 1, Re_S = 1070, Gr_S^* = 1.15 \times 10^6$ ($M \times N = 81 \times 141$).

Table 4
Effect of the height of the computational domain

| (H/L) | $\theta_{max}$ (Left/Right) | Percentage change (abs.) | $\overline{C}_f$ | Percentage change (abs.) |
|---|---|---|---|---|
| 1.0 | 0.248120 | – | 0.048030 | – |
| 1.5 | 0.248138 | 0.007 | 0.048129 | 0.21 |
| 2.0 | 0.248142 | 0.002 | 0.048136 | 0.02 |
| 2.5 | 0.248143 | 0.0004 | 0.048140 | 0.008 |

$A = 12, A_1 = A_2 = 5.25$ (heat sources at wall centers), $q_V = 10^6$ W/m$^3$, $\varepsilon = 0.45, k_s = 0.25$ W/m K, $k_f = 0.0291$ W/m K, $Ri_S^* = 1, Re_S = 1070, Gr_S^* = 1.15 \times 10^6$ ($M \times N = 81 \times 141$ and $N_1 = 91$).

formed using a grid pattern with $M = 81$, $N_1 = 91$ and $N = 141$.

### 3.2. Effect of height of the computational domain

To analyze the role, the height $H$ of the computational domain plays, results are obtained for the same typical case as considered above, by solving the problem using the computational domain of different heights. The results are provided in Table 4. It can be noticed that the difference in $\theta_{max}$ between $(H/L) = 2$ and 2.5 is only 0.0004%, while the difference in $\overline{C}_f$ between the same two values of $(H/L)$ is only 0.008%. Thus, a computational domain of height equal to twice the channel height (viz., $H = 2L$) is used for all the computations.

### 3.3. Check for mass and energy balance

The results of the present problem are tested for mass and energy balance in the entire mixed convection regime. As an example, for $A = 12$, $A_1 = A_2 = 5.25$ (heat sources at respective wall centers), $q_V = 10^6$ W/m$^3$, $k_s = 0.25$ W/m K, $\varepsilon = 0.45$ and $Gr_S^* = 10^5$, results are obtained for five values of $Ri_S^*$ (= 0.1, 0.25, 1, 10 and 25). Both the mass and energy balance are found satisfactory within ±0.1% and ±0.78%, respectively. Similar trends are seen in all the other cases too.

### 3.4. Validation

In order to validate the heat transfer results, the problem has been separately solved for the special case, wherein the two walls do not have heat sources and are isothermal. A set of 18 data has been generated encompassing the entire range of aspect ratios in the asymptotic free convection limit ($Ri_S^* = 25$). The average convection Nusselt number thus evolved is compared with the semi-empirical correlation of Elenbaas [1] and the analytical solution of Bar-Cohen and Rohsenow [3], both of which are for free convection in air in a vertical channel with symmetric isothermal walls. A fairly good agreement has been noticed with maximum deviations limited to within ±9.7% and ±8.6%, respectively.

### 3.5. Streamlines and isotherms for different regimes of mixed convection and for a given aspect ratio

Fig. 3 shows, respectively, (i) streamline and (ii) isotherm patterns for all the three regimes of mixed convection. They are (a) free convection dominant regime, $Ri_S^* = 25$ (b) mixed convection regime, $Ri_S^* = 1$ and (c) forced convection dominant regime, $Ri_S^* = 0.1$. The plots pertain to $A = 4, L_1 = L_2 = 7L/16$ (heat sources at respective wall centers), $q_V = 10^6$ W/m$^3$, $k_s = 1$ W/m K, $\varepsilon_L = \varepsilon_R = 0.45$ and $Gr_S^* = 10^6$. The streamlines exhibit a perfect symmetry in all the three regimes of mixed convection. They show a tendency to straighten up and move closer to each other with the nature of flow changing from free to forced convection dominance. With regard to isotherms too, there is a perfect symmetry in all the regimes of mixed convection. There is an expected crowding of isotherms near the heat source. Another noticeable feature is that the thermal boundary layers on the two walls get thinner gradually as one moves from the free to the forced convection limit, implying an increase in convection heat transfer in the channel. This, indeed, is found correct, with the relative contribution to heat transfer from convection increasing from about 36% to 66% as $Ri_S^*$ decreases from 25 to 0.1,

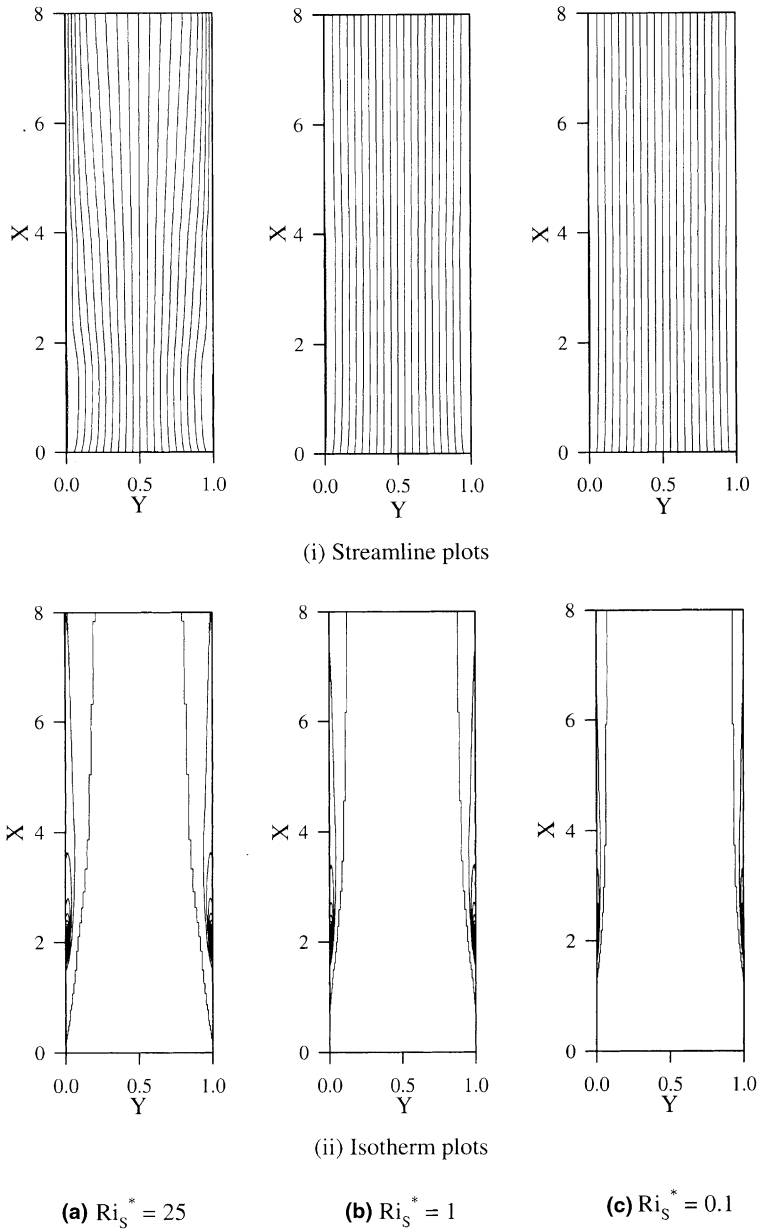


Fig. 3. Streamline and isotherm plots for all the three regimes of mixed convection for the case where both the walls have centrally located discrete heat sources [$A = 4$, $L_1 = L_2 = 7L/16, q_V = 10^6$ W/m$^3$, $k_s = 1$ W/m K, $\varepsilon_L = \varepsilon_R = 0.45$ and $Gr_S^* = 10^6$].

in this particular example. Incidentally, in this example, for $Ri_S^* = 1$, convection contributes 49% to the total heat transfer.

### 3.6. Streamlines and isotherms for different aspect ratios and for mixed convection regime

Fig. 4 shows two sets of contour plots, viz., (i) streamline and (ii) isotherm patterns for mixed convection regime ($Ri_S^* = 1$). The figure is for a representative case with $q_V = 10^6$ W/m$^3$, $k_s = 1$ W/m K, $\varepsilon_L = \varepsilon_R = 0.45$ and $L_1 = L_2 = 7L/16$ (two discrete heat sources at corresponding wall centers). Three aspect ratios $A = 4$, 12 and 20 have been considered in drawing the plots for the sake of clarity, note that these plots are not drawn to scale. It can be observed that both streamlines and isotherms show perfect symmetry for all the aspect ratios. As aspect ratio increases, the streamlines appear to move

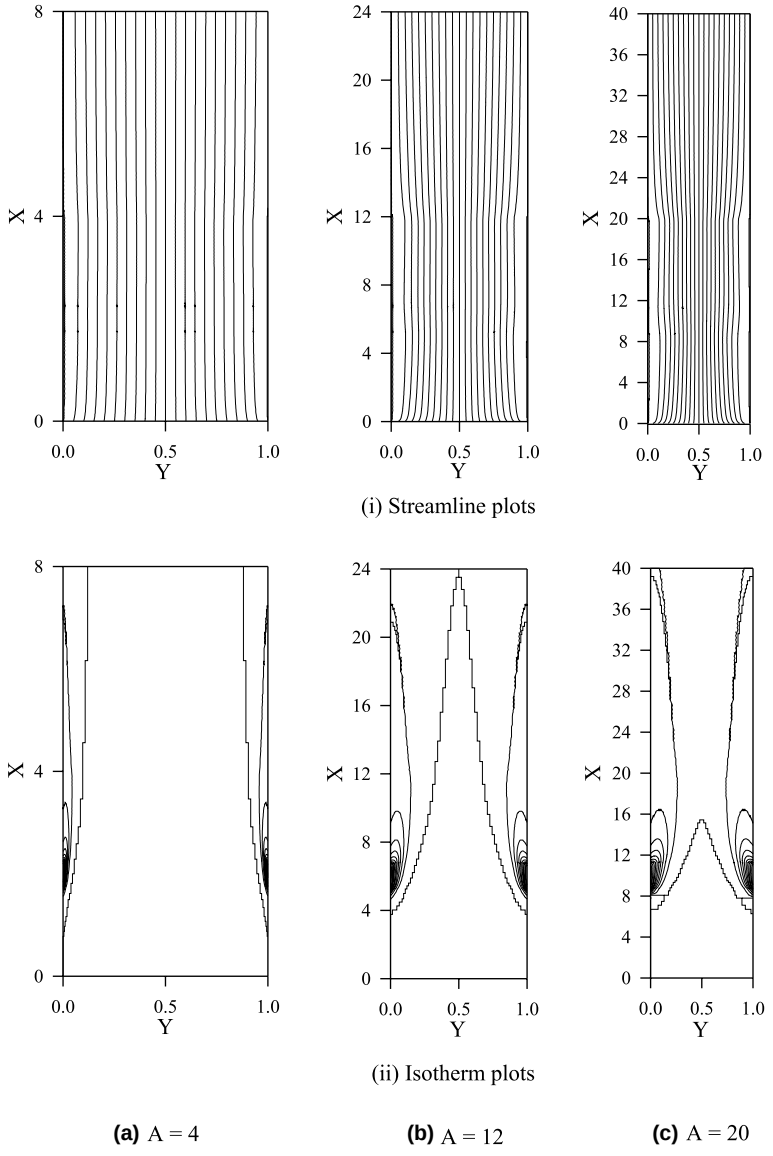


Fig. 4. Streamline and isotherm plots for three aspect ratios and for the case of mixed convection where both the walls have centrally located discrete heat sources [$L_1 = L_2 = 7L/16, q_V = 10^6$ W/m$^3$, $k_s = 1$ W/m K, $\varepsilon_L = \varepsilon_R = 0.45, Ri_S^* = 1$].

closer to each other, which would possibly mean an increase in mean friction coefficient and a consequent increase of pumping power requirement. Exploring this a little further, friction coefficient calculations are made for all three aspect ratios for this example. It is found that the mean friction coefficient does in fact increase by as much as 186% (from 0.0197 to 0.0563) with aspect ratio increasing from 4 to 20. With regard to isotherms, there is a crowding around the discrete heat source implying that most of the heat transfer takes place over there. Further, the thermal boundary layer does not seem to commence at the channel entry, and the starting length of the thermal boundary layer appears to be increasing with increasing aspect ratio. This would probably mean a decrease in heat transfer activity with increasing aspect ratio.

It can further be noted from Fig. 4 that, for $A = 4$, the channel simulates two isolated vertical plates, with two distinct, well defined, thermal boundary layers, which do not meet even at the top end of the extended computational domain ($X = 8$). For $A = 12$, the two thermal boundary layers meet each other just ahead of the top end of the domain ($X = 20$), but well beyond the channel exit ($X = 12$). However, for $A = 20$, the two

thermal boundary layers meet fairly early ($X = 14$), well ahead of the channel exit. These observations mean that there is a progressive decrease in convection heat transfer with an accompanying increase in wall temperature with increasing aspect ratio. In the present example, the convection heat transfer decreases by 12%, while the maximum wall temperature $\theta_{max}$ increases by about 8.4% as the aspect ratio increases from 4 to 20. It is thus not wise to go for very long channels for a given width or very narrow channels for a given height.

### 3.7. Variation of local wall temperature with other parameters

Fig. 5(a) and (b) show the non-dimensional local wall temperature profiles for $A = 4$, $q_V = 10^6$ W/m$^3$ and $k_s = 1$ W/m K. Fig. 5(a) depicts the wall temperature profiles in different regimes of mixed convection ($Ri_S^* = 25$, 1 and 0.1) for a given surface emissivity $\varepsilon_L = \varepsilon_R = 0.05$. Fig. 5(b) gives the wall temperature profiles for three different emissivities ($\varepsilon_L = \varepsilon_R = 0.05, 0.45$ and 0.85) in the mixed convection regime ($Ri_S^* = 1$). Both the plots pertain to the configuration, where the heat sources are at their respective wall centers, and hence walls have identical temperature profiles. It can be seen from Fig. 5(a) and (b) that the wall temperature shows a negligible rise up to the first quarter of the wall, from where the temperature increases sharply. The peak temperature always occurs near the center of the discrete heat source. From the maximum, the temperature drops again sharply to some lower value, before becoming asymptotic towards the channel exit.

One can also see from Fig. 5(a) that the local wall temperature decreases as one moves from $Ri_S^* = 25$ to $Ri_S^* = 0.1$, for a given wall emissivity. This is because of the increase in convection heat transfer as the flow changes from free to forced convection dominance. In the present example, the peak wall temperature decreases by about 11% as $Ri_S^*$ decreases from 25 to 0.1. Fig. 5(b) shows that the temperature at any location along the wall decreases with increasing surface emissivity. This is because the radiation heat transfer increases with $\varepsilon$ for a given set of other parameters and thus brings down the local wall temperature. In the present example, the peak wall temperature decreases by about 44% as $\varepsilon$ increases from 0.05 to 0.45, while it decreases by a further 17% with $\varepsilon$ increasing to 0.85 from 0.45.

In order to study the local wall temperature profiles, when the two heat sources are positioned at different locations along the walls, a family of curves has been drawn, as shown in Fig. 6. The figure pertains to $A = 4$, $q_V = 10^6$ W/m$^3$ and $k_s = 1$ W/m K and considers three cases. Case (1) is for $L_1 = L_2 = 0$ (both the heat sources commence from the channel entry). Case (2) pertains to $L_1 = 0$ and $L_2 = 7L/16$ (right wall heat source is at the wall center). Case (3) belongs to $L_1 = 0$ and $L_2 = 7L/8$ (right wall heat source ends at the channel exit). The two walls have identical temperature profiles, as expected, in case (1) owing to the identical position of the heat sources. In case (2), the left wall temperature profile remains largely unaffected, while the right wall temperature profile not only gets shifted in its position, but also reveals a slight increase in the peak wall temperature. Further, the right wall temperature in the upper half of

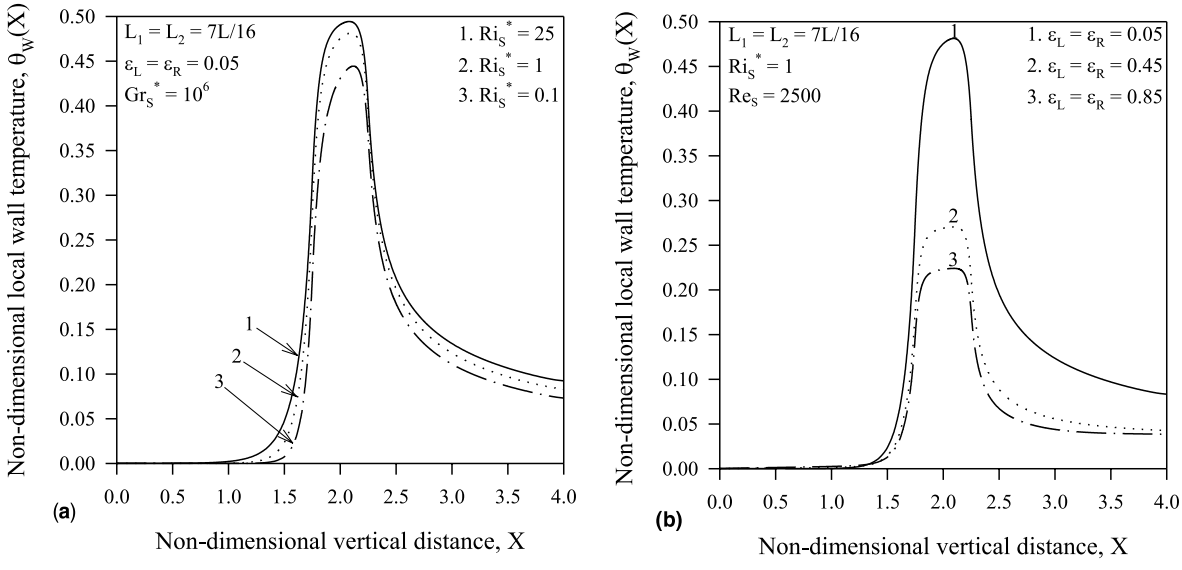


Fig. 5. Non-dimensional local wall temperature profiles (a) for different regimes of mixed convection and (b) for different surface emissivities [$A = 4$, $q_V = 10^6$ W/m$^3$ and $k_s = 1$ W/m K].

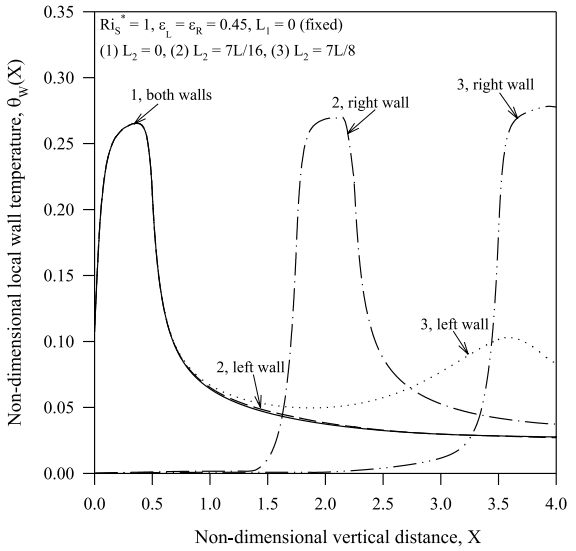


Fig. 6. Non-dimensional local wall temperature profiles for the case where the position of the right wall heat source is changed while the left wall heat source is held fixed [$A = 4$, $q_V = 10^6$ W/m$^3$ and $k_s = 1$ W/m K].

the channel is higher than that in case (1). In the present example, the temperature of the right wall at the channel exit increases by as much as 32% in case (2) compared to the corresponding value in case (1). However, the maximum temperature of the right wall increases a marginal 14% (by 2%) in comparison to that in case (1). In case (3), where the right wall heat source is at the channel exit, with the heat source in the left wall held fixed at the channel entry, the right wall temperature reaches its peak just a little before the exit of the channel. In the present example, the right wall peak temperature increases by about 6% compared to the case (1).

The left wall temperature shows an interesting feature in that it shows two peaks. Initially, like in the first two cases, the left wall temperature rises sharply to a maximum and comes down to a minimum, somewhere near the center of the wall. From here, instead of decreasing asymptotically with channel height like in cases (1) and (2), the temperature starts increasing yet again to a second peak that is smaller than the first peak, somewhere near the channel exit. Again, it decreases to a second minimum that is higher than the first minimum in the first two cases, the right wall temperature decreases in the second half of the channel, while in case (3) it begins to increase only in the second half. Because of this, the irradiation received by the left wall from the right wall increases in the second half of the channel. Hence the left wall temperature increases once again in the second half of the channel. In the example considered here, the second peak in the left wall temperature is about 61% less than its first peak, while the second minimum is about 67% higher than its first minimum. Fig. 6 also demonstrates that the best position for the heat source of the left or the right wall is the channel entry itself.

### 3.8. Variation of maximum wall temperature with other parameters

Fig. 7(a) shows the variation of $\theta_{max}$ with reference to $\varepsilon$ ($\varepsilon_L$ or $\varepsilon_R$) drawn for three typical values of $Ri_S^*$, viz., 25, 1 and 0.1 for $A = 12$, $L_1 = L_2 = 7L/16$, $q_V = 10^6$ W/m$^3$, $k_s = 0.25$ W/m K, and $Gr_S^* = 10^6$. Five values of $\varepsilon$ ($\varepsilon_L$ or $\varepsilon_R$) are chosen, viz., 0.05, 0.25, 0.45, 0.65 and 0.85. The figure reveals that $\theta_{max}$ decreases monotonically with increasing $\varepsilon$ for all values of $Ri_S^*$. This decrease is more pronounced in the free convection dominant regime ($Ri_S^* = 25$) than in the forced convection dominant regime ($Ri_S^* = 0.1$), while for the mixed convection regime ($Ri_S^* = 1$), the decrease in $\theta_{max}$ lies somewhere in between the two extremes. In the present example, when $\varepsilon$ increases from 0.05 to 0.85, $\theta_{max}$ decreases by 48% for $Ri_S^* = 25$, while for $Ri_S^* = 0.1$, it decreases by 37%. For $Ri_S^* = 1$, the decrease in $\theta_{max}$ between the same limits of $\varepsilon$ is by 45.5%. Fig. 7(a) further indicates that, for a given $\varepsilon$, $\theta_{max}$ decreases as $Ri_S^*$ decreases from 25 to 0.1. This is because, as $Ri_S^*$ decreases, the flow regime changes from free to forced convection dominance. This increases the rate of convection heat transfer, which, in turn, brings down the $\theta_{max}$. In the present example, for $\varepsilon = 0.45$, $\theta_{max}$ decreases by 21% as $Ri_S^*$ decreases from 25 to 0.1. The above study on variation of $\theta_{max}$ with reference to $\varepsilon$ and $Ri_S^*$, respectively, reveals that $\theta_{max}$ is a much stronger function of $\varepsilon$ than $Ri_S^*$. Fig. 7(a) also shows that the decrease in $\theta_{max}$ with decreasing $Ri_S^*$ is less significant in the free convection dominant regime than in the forced convection dominant regime. In the present example, for $\varepsilon = 0.05$, $\theta_{max}$ decreases by only 11% as $Ri_S^*$ decreases from 25 to 1. However, for the same $\varepsilon(= 0.05)$, the decrease in $\theta_{max}$ is by as much as 25% as $Ri_S^*$ decreases from 1 to 0.1.

Fig. 7(b) shows the variation of $\theta_{max}$ with aspect ratio ($A$) for $L_1 = L_2 = 7L/16$, $q_V = 10^6$ W/m$^3$, $k_s = 0.25$ W/m K and $\varepsilon_L = \varepsilon_R = 0.45$. The plot is for five typical values of $Ri_S^*$, viz., 25, 10, 1, 0.25 and 0.1. It can be noticed that for all values of $Ri_S^*$, $\theta_{max}$ increases as the aspect ratio increases from $A = 4$ to $A = 20$. However, for $Ri_S^* = 25$ and 10 (free convection dominant regime), there is a relatively milder increase in $\theta_{max}$ with $A$, in comparison to a rather larger rise as one moves towards the lower range of $Ri_S^*$ from 1 to 0.1 (forced convection dominant regime). In the present example, for $Ri_S^* = 25$, $\theta_{max}$ increases only marginally by 1.5% as the aspect ratio increases from 4 to 20. For $Ri_S^* = 1$ (mixed convection), $\theta_{max}$ increases by 4% as $A$ increases from 4 to 20. However, for $Ri_S^* = 0.1$, $\theta_{max}$ increases to a relatively higher value by about 11.5% for the same increase in

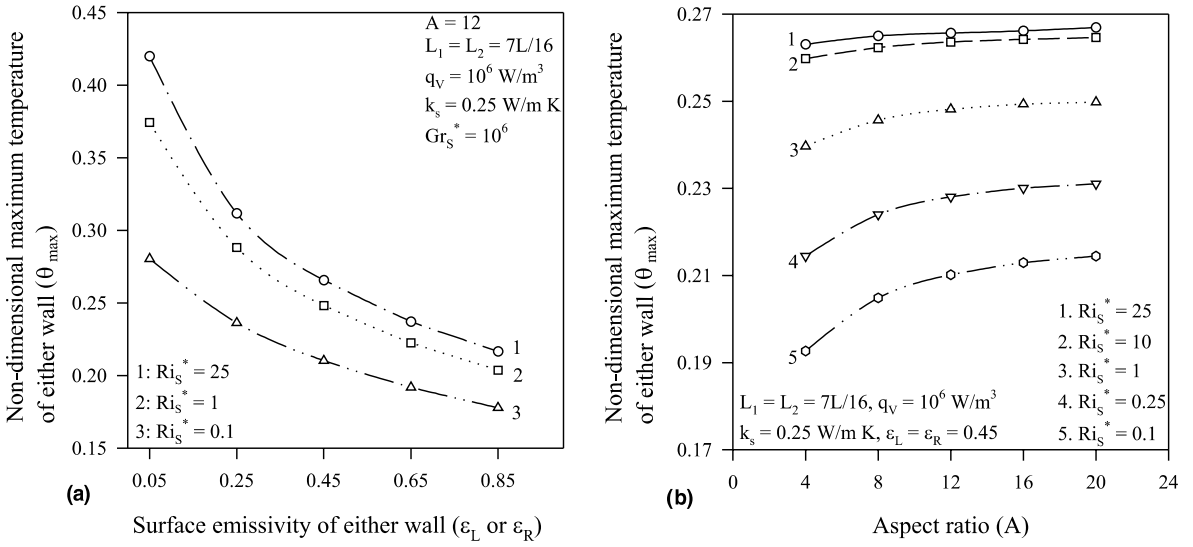


Fig. 7. Variation of non-dimensional maximum wall temperature with (a) surface emissivity of either wall in different mixed convection regimes and (b) aspect ratio for different modified Richardson numbers.

aspect ratio from 4 to 20. In view of the above, for a given wall height, it is not advisable to go for narrow channels in any regime of mixed convection. Fig. 7(b) also reveals that, for a given $A$, $\theta_{max}$ decreases with decreasing $Ri_S^*$, due to reasons already mentioned. In the present example, for $A = 12$, $\theta_{max}$ decreases by 21% as $Ri_S^*$ decreases from 25 to 0.1.

### 3.9. Variation of mean friction coefficient with other parameters

Knowledge of the variation of the mean friction coefficient $\overline{C}_f$ with other parameters is essential from an engineering viewpoint since the cost of pumping required to maintain the flow of air along the channel depends on it. In this context, Fig. 8(a) shows the variation of $\overline{C}_f$ with surface emissivity $\varepsilon$ of either wall for $A = 12$, and $Gr_S^* = 1.2 \times 10^6$. Fig. 8(b) shows the variation of $\overline{C}_f$ with aspect ratio $A$ for $\varepsilon_L = \varepsilon_R = 0.45$. The above plots have been drawn for different regimes of mixed convection for a representative case with $L_1 = L_2 = 7L/16, q_V = 10^6$ W/m$^3$ and $k_s = 0.25$ W/m K. Five surface emissivities $\varepsilon = 0.05, 0.25, 0.45, 0.65$ and 0.85 are considered as far as Fig. 8(a) is concerned, while five aspect ratios $A = 4$, 8, 12, 16 and 20 have been used for Fig. 8(b).

Fig. 8(a) indicates that the decrease in $\overline{C}_f$ with increasing $\varepsilon$ ($\varepsilon_L$ or $\varepsilon_R$) is quite small in the forced convection dominant regime ($0.1 \leqslant Ri_S^* < 1$), while, in the free convection dominant regime ($1 < Ri_S^* \leqslant 25$), $\overline{C}_f$ decreases substantially with increasing $\varepsilon$. In the present example, for $Ri_S^* = 0.1$, $\overline{C}_f$ decreases only marginally by 2%, while for $Ri_S^* = 25$, the decrease would be by as much as 45.5%, as $\varepsilon$ increases from 0.05 to 0.85. Fig. 8(b) shows that, as the aspect ratio increases, $\overline{C}_f$ increases too. However, the increase is more significant in the forced convection dominant regime ($0.1 \leqslant Ri_S^* < 1$), than in the free convection dominant regime ($1 < Ri_S^* \leqslant 25$). Further, there is an almost linear increase in $\overline{C}_f$ in the forced convection dominant regime. In the example pertaining to Fig. 8(b), for $Ri_S^* = 0.1$, $\overline{C}_f$ increases by 149%, while for $Ri_S^* = 25$, the increase in $C_f$ is by a comparatively lower 129%. Since an increase of $\overline{C}_f$ implies an increase in the pumping cost, the use of tall narrow channels is not to be preferred in practical applications.

### 3.10. Isolating the role of surface radiation

In order to isolate the role of surface radiation in the present problem results have been obtained with and without surface radiation accounted for. Fig. 9(a) shows the variation of $\theta_{max}$ and $\theta_{av}$, while Fig. 9(b) shows the variation of $\overline{C}_f$ with $Ri_S^*$, for $\varepsilon_L = \varepsilon_R = 0.85$ and $\varepsilon_L = \varepsilon_R = 0$. The curves are for $A = 12$, $L_1 = L_2 = 7L/16, q_V = 10^6$ W/m$^3$, $k_s = 0.25$ W/m K and $Gr_S^* = 1.2 \times 10^6$, and for five typical values of $Ri_S^* = 0.1$, 0.25, 1, 10 and 25. Fig. 9(a) reveals that, when surface radiation is ignored, both $\theta_{max}$ and $\theta_{av}$ increase, for all values of $Ri_S^*$, compared to the results obtained, when radiation is taken into account. The increase in $\theta_{max}$ and $\theta_{av}$ is the least in the forced convection limit and the largest in the free convection limit. In the example here, when radiation is ignored, $\theta_{max}$ increases by 68% for $Ri_S^* = 0.1$, while for $Ri_S^* = 25$, it increases by 129%, compared to the results obtained when radiation is considered. With

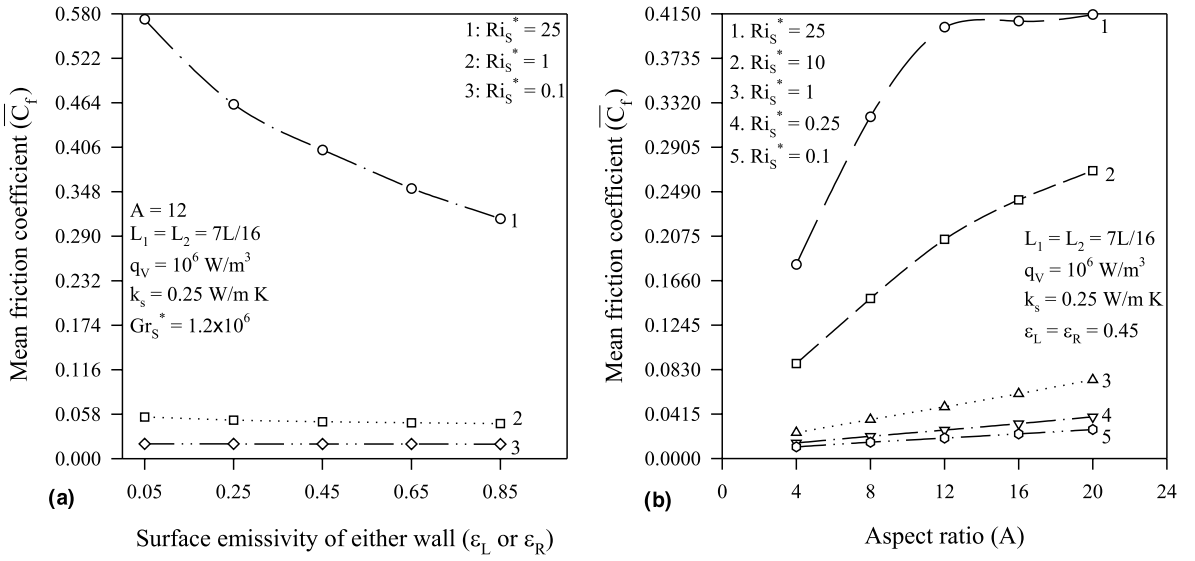


Fig. 8. Variation of mean friction coefficient with (a) surface emissivity of either wall and (b) aspect ratio in different regimes of mixed convection.

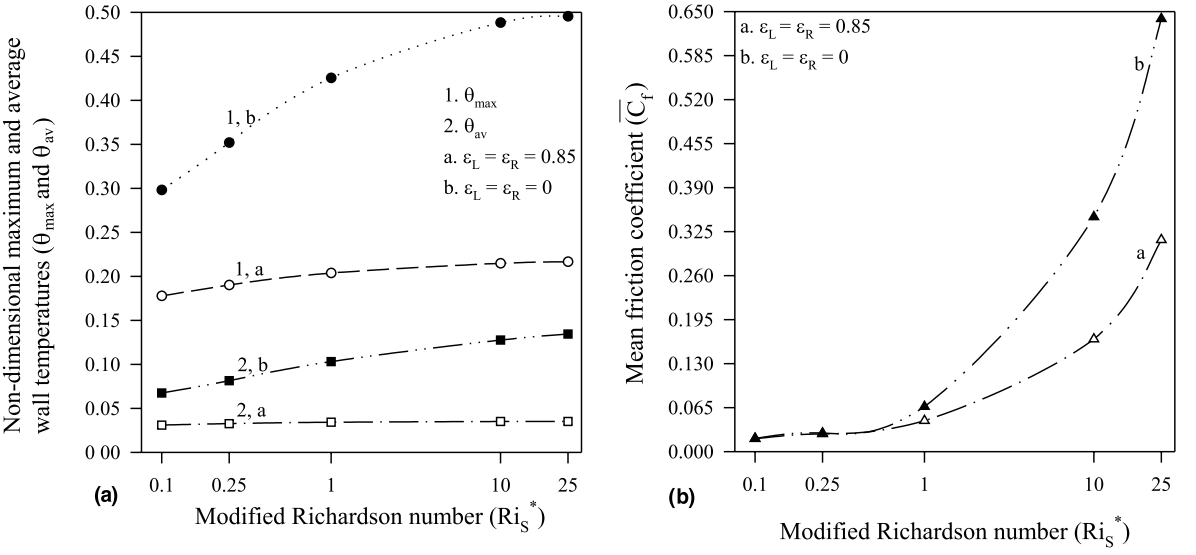


Fig. 9. Comparison of (a) non-dimensional maximum and average wall temperatures and (b) mean friction coefficient, with and without surface radiation, for different modified Richardson numbers [$A = 12$, $L_1 = L_2 = 7L/16, q_V = 10^6$ W/m$^3, k_s = 0.25$ W/m K and $Gr_S^* = 1.2 \times 10^6$].

regard to $\theta_{av}$, when radiation is not taken into account, there is an increase of 116%, for $Ri_S^* = 0.1$, and of 283%, for $Ri_S^* = 25$, compared to the results when radiation is accounted for. Fig. 9(b) shows that, for forced convection dominant regime, radiation has negligible influence on $\overline{C}_f$. In the free convection dominant regime, radiation gains significance, decreases $\overline{C}_f$ considerably, and thus brings down the pumping cost. In the present case, for $Ri_S^* = 0.1$, $\overline{C}_f$ increases by just 2%, if radiation is not accounted for, compared to the result obtained with radiation. For $Ri_S^* = 25$, the increase in $\overline{C}_f$ in the absence of radiation is by as much as 104%.

### 3.11. Contributions by convection and radiation to total heat transfer

In the present problem, the volumetric heat generation $q_V$ in each heat source is known a priori. This

implies that the total heat load is fixed. The question now would be to know the relative contributions of convection (free and forced) and radiation to the total heat transfer in the channel. Figs. 10(a) and (b) show the relative contributions of convection and radiation to the total heat transfer plotted against wall emissivity [for $A = 12$ and $Gr_S^* = 1.2 \times 10^6$] and aspect ratio [for $\varepsilon_L = \varepsilon_R = 0.45$], respectively. Both the Figs. 10(a) and (b) pertain to $L_1 = L_2 = 7L/16, q_V = 10^6$ W/m$^3$ and $k_s = 0.25$ W/m K and are drawn for three values of $Ri_S^*$, viz., 25, 1 and 0.1.

Fig. 10(a) shows a monotonic decrease in the contribution from convection, with a proportionate increase in that from radiation, for all values of $Ri_S^*$, as $\varepsilon$ increases from 0.05 to 0.85. In this example, for $Ri_S^* = 25$ (free convection limit), for $\varepsilon = 0.05$, convection contributes about 77% to heat transfer, with only 23% of heat dissipated through radiation. For $\varepsilon = 0.85$, on the other hand, convection is weak providing only 20% of heat transfer, with the remaining 79.5% coming from radiation. Further, for this case ($Ri_S^* = 25$), at $\varepsilon \approx 0.2$, the contributions from convection and radiation become equal and the curves therefore cross each other. For $Ri_S^* = 0.1$ (forced convection limit), for $\varepsilon = 0.05$, the convection contribution is 92%, with radiation giving only 7.5%. Even when $\varepsilon = 0.85$, convection contributes as much as 44% to heat transfer, with radiation providing 55.5%. In this case ($Ri_S^* = 0.1$), at $\varepsilon \approx 0.7$, the two curves cross each other, which indicates equal contributions to heat transfer from convection and radiation. For the mixed convection regime, $Ri_S^* = 1$, as can be seen, the trends of the curves related to convection and radiation are in between the above extremes, with the cross over taking place at $\varepsilon \approx 0.35$. In summary, the surface is a poor emitter ($\varepsilon = 0.05$), radiation contributes a maximum of only 20–25% to heat transfer. For all other surfaces ($\varepsilon > 0.05$), radiation plays a key role and therefore cannot be ignored.

It can be seen from Fig. 10(b) that the contribution by convection decreases as the aspect ratio increases, for all values of $Ri_S^*$. In the present example, for $Ri_S^* = 25$, the contribution by convection is 35.5% for $A = 4$, and this comes down to 31.5% for $A = 20$, while an exact and opposite change takes place for the radiation heat transfer. It is also apparent from Fig. 10(b) that, for the case of $Ri_S^* = 25$, for all the aspect ratios (4–20), the radiation heat transfer is more than 60%. For $Ri_S^* = 0.1$, on the contrary, convection is dominant for all aspect ratios, and is 66% for $A = 4$, which decreases only to 58.5% for $A = 20$. The radiation contribution will be comparatively low at 34.9% for $A = 4$ and 41% for $A = 20$. Trends for $Ri_S^* = 1$ fall in between the two extremes.

### 3.12. Effect of position of the discrete heat source

In order to study the effect of the position of the heat source, two families of curves have been drawn, as shown in Fig. 11. The plots pertain to $A = 12$, $q_V = 10^6$ W/m$^3$, $k_s = 0.25$ W/m K, $\varepsilon_L = \varepsilon_R = 0.45$ and $Gr_S^* = 10^6$, and are shown for all the three regimes of mixed convection. The positions of the two discrete heat sources are changed ensuring that they will always be at identical positions in their respective walls. Fig. 11(a) shows the nature of variation of $\theta_{max}$, while Fig. 11(b) shows the relative contributions of convection and

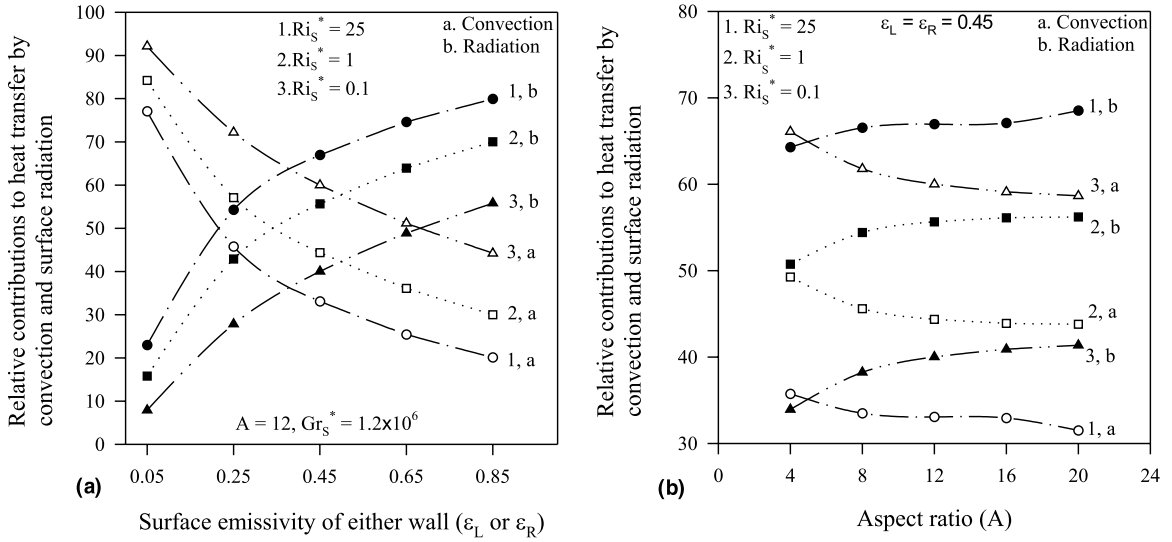


Fig. 10. Relative contributions to heat transfer from convection and surface radiation with reference to (a) surface emissivity and (b) aspect ratio in different mixed convection regimes [$L_1 = L_2 = 7L/16, q_V = 10^6$ W/m$^3$, $k_s = 0.25$ W/m K].

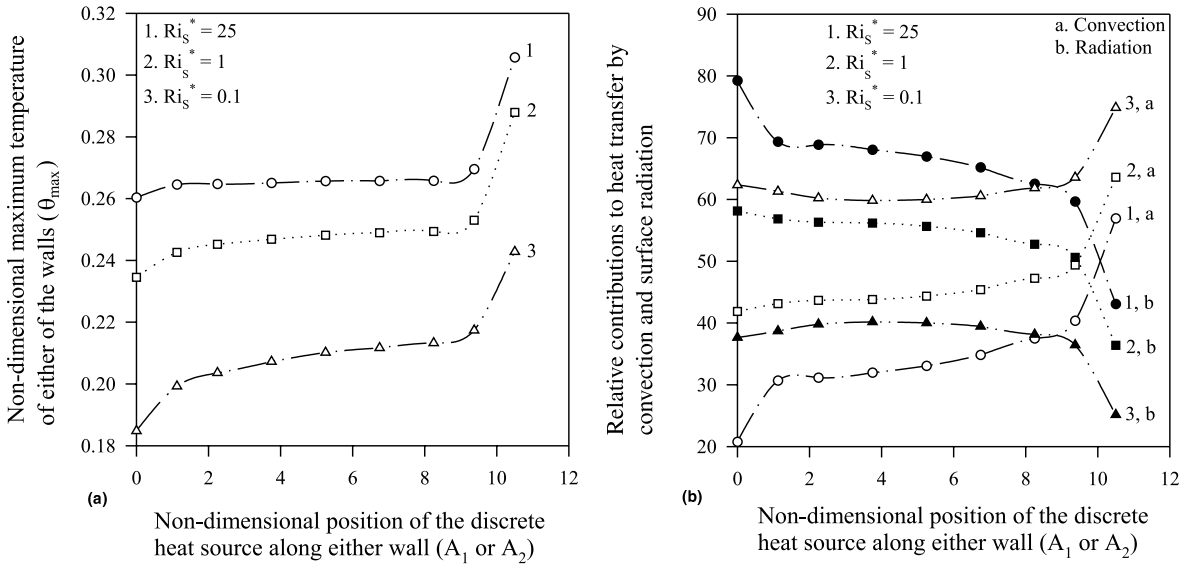


Fig. 11. Variation of (a) non-dimensional maximum wall temperature and (b) relative contributions of convection and radiation to heat transfer with non-dimensional heat source position in different regimes of mixed convection [$A = 12$, $q_V = 10^6$ W/m$^3$, $k_s = 0.25$ W/m K, $\varepsilon_L = \varepsilon_R = 0.45$ and $Gr_S^* = 10^6$].

radiation to heat transfer, with reference to the non-dimensional heat source position along either wall ($A_1$ or $A_2$). It is to be noted that, since the height of the heat source in the present study is taken to be ($L/8$), the maximum possible value for $A_1$ (or $A_2$) would be $7L/8$. Since in this example, $A = 12$, the non-dimensional height of the heat source would be 1.5, and thus the maximum possible value for $A_1$ (or $A_2$) would be 10.5.

It can be inferred from Fig. 11(a) that $\theta_{max}$ increases as the heat source shifts from the entry ($A_1$ or $A_2 = 0$) to the exit ($A_1$ or $A_2 = 10.5$) of the channel. Initially, as the heat source moves from $A_1 = A_2 = 0$ to 1.125, $\theta_{max}$ increases to some high value, and from this position, up to $A_1 = A_2 = 9.375$, $\theta_{max}$ undergoes a mild increase. But, when the heat source moves to its topmost position, i.e., the exit of the channel ($A_1 = A_2 = 10.5$), there is a sudden and substantial jump in $\theta_{max}$. It can further be noticed that the extent of increase of $\theta_{max}$ between the heat source positions, $A_1 = A_2 = 1.125$ and 9.375, is less pronounced in the free convection dominant regime than in the forced convection dominant regime. For the mixed convection regime, $Ri_S^* = 1$, the trend lies somewhere in between the two extremes. In the example pertaining to Fig. 11(a), for $Ri_S^* = 25$, $\theta_{max}$ increases by about 2% between the positions $A_1 = A_2 = 0$ and 1.125, and by another 1.5% only between $A_1 = A_2 = 1.125$ and 9.375. However, the increase is as much as 13.5%, when the heat source moves from $A_1 = A_2 = 9.375$ to 10.5. For $Ri_S^* = 0.1$, the increase in $\theta_{max}$ is 8% between $A_1 = A_2 = 0$ and 1.125, and another 9% between $A_1 = A_2 = 1.125$ and 9.375. However, $\theta_{max}$ increases rather sharply by 11.5% with the heat source reaching its topmost position ($A_1 = A_2 = 10.5$). To summarize, $\theta_{max}$ increases by 17.5% as the heat source is shifted from the entry to the exit of the channel for $Ri_S^* = 25$, while between the same heat source positions, the increase in $\theta_{max}$ is by as much as 31% for $Ri_S^* = 0.1$. For the mixed convection regime ($Ri_S^* = 1$), the trends lie between the above two cases, with an increase of 23% in $\theta_{max}$ between the two extreme heat source locations. The above exercise thus concludes that the best position for the heat source is the entry of the channel ($A_1 = A_2 = 0$).

Fig. 11(b) shows that the contribution by convection to heat transfer increases with a proportionate decrease in that by radiation, as the heat source moves from the entry to the exit of the channel for $Ri_S^* = 25$ and 1. However, for $Ri_S^* = 0.1$, the contribution from convection decreases initially, and after a particular position for the discrete heat source, it starts increasing, with the variation in the contribution of radiation showing an opposite trend. For this case when $Ri_S^* = 25$, the contribution by convection increases from 21% to 57%, while that by radiation decreases from 79% to 43%, as the heat source moves from the entry to the exit of the channel. For $Ri_S^* = 1$, between the same extreme heat source positions, the contribution by convection increases from 42% to 64%, while radiation decreases from 58% to 36%. However, for $Ri_S^* = 0.1$, the contribution by convection initially decreases from 62% (for $A_1 = A_2 = 0$) to 60% (for $A_1 = A_2 = 3.75$). From here, it increases again to as much as 75% as the heat

source reaches its topmost position of the channel exit ($A_1 = A_2 = 10.5$). As may be expected, since the case $Ri_S^* = 0.1$ pertains to the forced convection limit, radiation is found to be much lower, with its contribution dropping from 38%, when the heat source is at the channel entry, to 25%, when the heat source ends on the channel exit.

### 3.13. Correlations

About 325 numerical data are generated, encompassing the range of parameters listed in Table 1. These results are used to develop the correlations for the non-dimensional maximum of the left and right walls of the channel and the mean friction coefficient.

The correlation for $\theta_{max}$ of either the left or the right wall of the channel, based on 281 data, is:

$$\theta_{max} = 8.1A^{-0.31}(1+\varepsilon)^{-1.12}(1+A_1)^{a}(1+A_2)^{b}\gamma^{-0.5} \times \left(\frac{N_{RF}}{1+N_{RF}}\right)^{0.54} \times (1+Ri_S^*)^{-0.07}Re_S^{-0.15} \quad (8)$$

Eq. (8) has a correlation coefficient of 0.996. This gives $\theta_{max}$ for the left wall when the exponents $a$ and $b$ are assigned, respectively, the values 0.03 and 0.01, within an error band of ±3%. For the right wall, the same equation would give $\theta_{max}$, within a maximum deviation of ±3.5%, just by interchanging the values of the exponents $a$ and $b$, i.e., by taking $a = 0.01$ and $b = 0.03$. In evolving Eq. (8), $(1+\varepsilon)$ has been chosen as an appropriate form for $\varepsilon$, because, even when $\varepsilon = 0$, implying no surface radiation, $\theta_{max}$ will still be non-zero as convection and wall conduction would be present. Since the non-dimensional left or right wall heat source position ($A_1$ or $A_2$) may vary from 0 to 17.5 (see Table 1), $(1+A_1)$ and $(1+A_2)$ are chosen to be the most appropriate forms for $A_1$ and $A_2$, respectively. For $Ri_S^*$, the form $(1+Ri_S^*)$ has been found more apt because even when there is no free convection ($Ri_S^* = 0$), $\theta_{max}$ is non-zero on account of forced convection and also surface radiation (provided $\varepsilon \neq 0$). The form for $N_{RF}$, however, is chosen mainly to minimize the error in its exponent in the correlation, and thus improve the overall correlation coefficient.

Separate correlations have been found necessary for $\overline{C}_f$ covering the ranges of low and high $Ri_s^*$ viz., $0.1 \leqslant Ri_S^* \leqslant 1$ and $1 < Ri_S^* \leqslant 25$, respectively, because a single correlation for the entire range ($0.1 \leqslant Ri_S^* \leqslant 25$) that shows a good agreement with the data could not be found. $\overline{C}_f$, based on both the walls of the channel, for low modified Richardson number range ($0.1 \leqslant Ri_S^* \leqslant 1$), has been correlated using 188 data that pertain to the Reynolds number range ($100 \leqslant Re_S \leqslant 27500$). The correlation thus developed has a correlation coefficient of 0.994 and an error band of ±3.5%, and is

$$\overline{C}_f = 3.34A^{-0.12}(1+\varepsilon)^{-0.18}(1+A_1)^{-0.03}(1+A_2)^{-0.02} \times \gamma^{-0.07}\left(\frac{N_{RF}}{1+N_{RF}}\right)^{0.13} \times (1+Ri_S^*)^{0.55}Re_S^{-0.55}. \quad (9)$$

The correlation for $\overline{C}_f$ pertaining to the high modified Richardson number range ($1 < Ri_S^* \leqslant 25$) has been derived based on 102 data that covers the range ($25 \leqslant Re_S \leqslant 4000$). This correlation has a correlation coefficient of 0.991 with an error band of ±4.5% and is:

$$\overline{C}_f = 1.92A^{-0.15}(1+\varepsilon)^{-1.3}(1+A_1)^{-0.03}(1+A_2)^{-0.01} \times \gamma^{-0.2}\left(\frac{N_{RF}}{1+N_{RF}}\right)^{0.2} \times (1+Ri_S^*)^{0.56}Re_S^{-0.38}. \quad (10)$$

### 3.14. Forced convection friction coefficient component

Eqs. (9) and (10) give the sum of free and forced convection components of $\overline{C}_f$. Of these, only the forced convection component of $\overline{C}_f$ makes a demand on the pumping power. An examination of the data showed that forced convection dominant solution was valid for $Ri_s^* < 0.1$. When Eq. (9) is extrapolated to $Ri_s^* = 0$, we get a value which is in close agreement with the value obtained by running the program by setting $\beta = 0$. As many as 28 raw data obtained by setting = 0 showed that Eq. (9) with $Ri_s^* = 0$ is a good representation of $\overline{C}_f$ in the absence of free convection and thus represents the forced convection component.

## 4. Conclusions

The salient conclusions from the present study are:

1. The local, maximum and average wall temperatures decrease with surface emissivity. The peak wall temperature is found to come down by 50% or even more as the wall surface changes from a good reflector to a good emitter.
2. Both $\theta_{max}$ and $\theta_{av}$ decrease as $Ri_S^*$ decreases from 25 to 0.1. However, both $\theta_{max}$ and $\theta_{av}$ have been found to be showing a much stronger dependence on $\varepsilon$ compared to $Ri_S^*$.
3. For all the values of $Ri_S^*$, both $\theta_{max}$ and $\theta_{av}$ increase with aspect ratio. The increase is relatively mild in the free convection dominant regime and rather sharp in the forced convection dominant regime.
4. $\overline{C}_f$ decreases with increasing $\varepsilon$, minimally (2–5%) in the forced convection dominant regime and substantially (45–50%) in the free convection dominant regime.
5. $\overline{C}_f$ increases with increasing aspect ratio, almost linearly and also more significantly (125–150%) in the forced convection dominant regime ($0.1 \leqslant Ri_S^* < 1$), while in the free convection dominant regime

($1 < Ri_S^* \leqslant 25$), the increase is comparatively to a lower extent (100–125%).

6. A monotonic decrease in contribution from convection to heat transfer in the channel with a proportionate increase in its radiation counterpart is noticed for all the values of $Ri_S^*$ with $\varepsilon$ increasing from 0.05 to 0.85. Contribution from convection to heat transfer decreases with a proportionate increase in that from radiation as the aspect ratio increases for all values of $Ri_S^*$.
7. $\theta_{max}$ increases as the heat source moves from the entry to the exit of the channel in all the three regimes of mixed convection.

## References


[1] W. Elenbaas, Heat dissipation of parallel plates by free convection, Physica 9 (1942) 1–28.

[2] L.N. Tao, On combined free and forced convection in channels, ASME J. Heat Transfer 82 (1960) 233–238.

[3] A. Bar-Cohen, W.M. Rohsenow, Thermally optimum spacing of vertical natural convection cooled parallel plates, ASME J. Heat Transfer 106 (1984) 116–123.

[4] A. Barletta, Laminar mixed convection with viscous dissipation in a vertical channel, Int. J. Heat Mass Transfer 41 (1998) 3501–3513.

[5] A.A. Dehghan, M. Behnia, Combined natural convection–conduction and radiation heat transfer in a discretely heated open cavity, ASME J. Heat Transfer 118 (1996) 56–64.

[6] C. Gururaja Rao, C. Balaji, S.P. Venkateshan, Conjugate mixed convection with surface radiation from a vertical plate with a discrete heat source, ASME J. Heat Transfer 123 (2001) 698–702.

[7] N.K. Anand, S.H. Kim, W. Aung, Effect of wall conduction on free convection between asymmetrically heated vertical plates: uniform wall temperature, Int. J. Heat Mass Transfer 33 (1990) 1025–1028.

[8] S.H. Kim, N.K. Anand, W. Aung, Effect of wall conduction on free convection between asymmetrically heated vertical plates: uniform wall heat flux, Int. J. Heat Mass Transfer 33 (1990) 1013–1023.

[9] S.H. Kim, N.K. Anand, L.S. Fletcher, Free convection between series of vertical parallel plates with embedded line heat sources, ASME J. Heat Transfer 113 (1991) 108–115.

[10] J.C. Watson, N.K. Anand, L.S. Fletcher, Mixed convective heat transfer between a series of vertical parallel plates with planar heat sources, ASME J. Heat Transfer 118 (1996) 984–990.

[11] A. Bejan, in: Convection Heat Transfer, first ed., Wiley-Interscience, New York, 1984, pp. 109–158.

[12] A.D. Gosman, W.M. Pun, A.K. Runchal, D.B. Spalding, M. Wolfshtein, in: Heat and Mass Transfer in Recirculating Flows, first ed., Academic Press, London and New York, 1969, pp. 89–137.

[13] P.J. Roache, in: Computational Fluid Dynamics, first ed., Hermosa, Albuquerque, New Mexico, USA, 1972, pp. 15–207.

[14] R. Siegel, J.R. Howell, in: Thermal Radiation Heat Transfer, third ed., Taylor & Francis, Washington and London, 1992, pp. 189–252.

[15] G.P. Peterson, A. Ortega, Thermal control of electronic equipment and devices, in: J.P. Hartnett, T.F. Irvine Jr. (Eds.), Advances in Heat Transfer, Academic Press, San Diego, California, 1990, pp. 181–314.